Academic Journal of Computing & Information Science
ISSN 2616-5775 Vol. 3, Issue 3: 117-128, DOI: 10.25236/AJCIS.2020.030313

Geometric Calibration of Freehand Ultrasound System with Electromagnetic Tracking

Jingbo Rong[1], Yaosheng Lu[2,*], Shucheng Qin[2], Rongdan Zeng[2]

[1]*Guangzhou Lian-Med Technology Ltd, Guangzhou 510663, China*
[2]*College of Information Science and Technology, Jinan University, Guangzhou 510632, China*
[*]*Corresponding Author: tluys@jnu.edu.cn*

ABSTRACT. *Geometric calibration aims to determine the transformation between the ultrasound image plane coordinate system and the sensor coordinate system attached to the probe. In order to solve the problem of obtaining high-accuracy and robust results intended for labor guidance usage, this study designed an automatic freehand ultrasound calibration system with minimal human interaction combined with electromagnetic tracking. In this system, a multilayer N-wire phantom was utilized, and an auxiliary bracket was designed to hold the ultrasound probe during data collection. Moreover, a completely automatic algorithm was proposed for fast image segmentation. Calibration quality was validated by calculating precision and accuracy. Results Extensive trials were also conducted. On average, the calibration accuracy was 1.42 mm, and the precision was 1.29 mm. These results suggest that precision and accuracy achieved with optimized multilayer N-wire phantoms can be more precise compared to other methods. Furthermore, the high-accurate and robust results demonstrate the freehand 3D ultrasound system can accurately track target anatomy during labor guidance.*

KEYWORDS: *Calibration, Electromagnetic tracking, Ultrasound, N-wire phantom*

1. Introduction

Three-dimensional (3D) ultrasound imaging is attracting growing interest in state-of-the-art monitoring fetal development applications. Knowing the precise position of the fetus and other labor parameters can help doctors to carry out necessary interventions [1] and prevent a variety of fetal syndromes. These labor parameters can be obtained by a 3D ultrasound system, which is usually achieved in two ways. The first method is to scan with an integrated volume probe, which has a small field of view and is not suitable for measuring very large targets. The second method is freehand scanning. Due to its safety, non-invasive and real-time imaging in any direction, it has attracted much attention in recent years. The freehand 3D ultrasound system calculates the position and orientation of the sensor when obtaining a set of 2D ultrasound images. However, the 3D coordinates of the

ISSN 2616-5775 Vol. 3, Issue 3: 117-128, DOI: 10.25236/AJCIS.2020.030313

ultrasonic image need to be determined by ultrasonic geometric calibration, which is the conversion between the ultrasonic image plane coordinate system and the probe sensor coordinate system.

Ultrasound geometric calibration plays such a key role in a freehand 3D ultrasound system. Hence, much research in recent decades has focused on calibration techniques. Calibration categories comprise single-point target and cross-wire phantom [2], which is the simplest and earliest phantom; multiple-point target and cross-wire phantom [3, 4] whose calibration process requires coplanarity of the ultrasonic plane surface with the target point, which results in a high demand for an operator; three-wire phantom [5], which consists of three lines perpendicular to one another; N-wire phantom [6-8] that consists of a pair of parallel lines and a straight line, which intersects the parallel lines.

Our research aimed to determine an optimized calibration solution to address the concerns for labor guidance usage in recent literature. We designed a multilayer N-wire phantom that needs few images to obtain accurate calibration result. To avoid the error and additional time cost caused by temporal calibration, an auxiliary bracket was designed to hold the ultrasound probe. This bracket also allowed the probe to move freely through the phantom, pause in arbitrarily desired position, and maintain the same pose to collect data. We also evaluated the precision and accuracy of our method and provided comparison with existing solutions.

2. Materials and Methods

2.1 System Overview

The ultrasound probe was tracked by an electromagnetic tracking system. To identify and extract all the central pixel coordinates of the points of intersection with the N-wires (N-fiducials) in each ultrasound image, an improved completely automatic image segmentation algorithm was carried out. With all segmented ultrasound images serving as input, the acquired pixel coordinate data and the probe location data were used to compute the calibration parameters. When the calibration parameters were determined, their precision and accuracy were calculated.

Fig. 1. Hardware components of the calibration system. (a) an electromagnetic tracking system, (b) an ultrasound machine, (c) a central notebook, (d) an

ISSN 2616-5775 Vol. 3, Issue 3: 117-128, DOI: 10.25236/AJCIS.2020.030313

electromagnetic transmitter, and (e) a R60 convex array probe with an attached position sensor.

Fig.1 shows the hardware components necessary in designing our automatic calibration system. We used an ultrasound machine (Color Doppler Ultrasound D6, Well.D Medical Electronics Co., Ltd., Shenzhen, Guangdong, China) to acquire and digitally store images. A R60 convex array probe (35C60CN, Well.D Medical Electronics Co., Ltd., Shenzhen, Guangdong, China) with a frequency of 3.5 MHz was used to scan the N-wire phantom by a software installed in the ultrasound machine. A square cross-section position sensor (Model 800, Ascension Technology Corp, Shelburne, VT, USA) attached to the probe was tracked by an electromagnetic tracking system (trakSTAR, Ascension Technology Corp., Shelburne, VT, USA). A cylindrical sensor (Model 180, Ascension Technology Corp., Shelburne, VT, USA) was also used to obtain the spatial location of the phantom. The electromagnetic signals emitted by an electromagnetic transmitter (Mid-range Transmitter, Ascension Technology Corp., Shelburne, VT, USA), which established tracking volumes, were tracked by all tracking components that were subjected to a calibration procedure; this step optimized the performance over a given region referred to as the performance motion box. The dimensions defined in each axis were as follows: X=20cm to 66 cm from the transmitter center, Y=±28 cm from the transmitter center, and Z=±30 cm from the transmitter center (Ascension Technology Corp.).

2.2 Multilayer n-Wire Phantom

The multilayer N-wire phantom consisted of a rectangular open flume (35 cm×35 cm×50 cm), which was made of five acrylic plates with thickness of 5 mm, as shown in Fig.2a. Precisions with round holes (20 lines with 24 holes each line) were drilled on both the front and back plates of the flume to mount all the N-wires (Nylon wires with a diameter of 0.28 mm). All holes showed a diameter of 1.5 mm, and the horizontal and vertical separations of the circular holes were set to 10 mm. To ensure that N-fiducials covered the ultrasound image area, which was a fan-shaped area produced by the convex array probe used, the multilayer N-wires were arranged from top to bottom according to the following widths: 7, 7, 9, 9, 11, 11, and 13 cm. Each layer contained a double N-wire, which differed in width by 10 mm and exhibited the same diagonal direction.

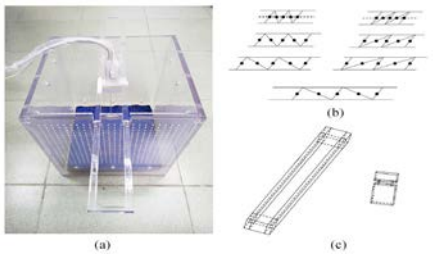

ISSN 2616-5775 Vol. 3, Issue 3: 117-128, DOI: 10.25236/AJCIS.2020.030313

Fig. 2. Design of the multilayer N-wire phantom and auxiliary bracket. (a) Overall view of the phantom (35 cm×35 cm×50 cm) and the auxiliary bracket, (b) specification design of the multilayer N-wires, and (c) components of the auxiliary bracket.

An auxiliary bracket was designed to hold the ultrasound probe, as shown in Fig.2a. In the actual image, a large angle between the ultrasound plane and the N-wire plane resulted in large lateral width of the dots. Consequently, the tracking error of the dots extracted by the automatic image segmentation and registration algorithm was high. When the ultrasound plane was substantially perpendicular to the N-wire plane, the dots appeared in the highest brightness from which they can be best identified. Hence, an auxiliary bracket, which consisted of two parallel rods and a retainer plate embedded between the rods and kept approximately orthogonal to the two rods, was needed (Fig.2c).

2.3 Data Acquisition

In order to ensure that the N reference appears as a bright spot in the ultrasound image, the phantom was placed in a transparent water bath. A piece of sound-absorbing sponge with a certain thickness and the same size as the bottom plate of the phantom was placed on the plate to absorb a large amount of ultrasonic energy and provide high-quality images. Three acrylic sticks were also embedded in the phantom above the sponge to prevent the sponge from rising off the plate due to buoyancy. The ultrasound probe with the attached position sensor was firmly affixed to the plate of the auxiliary bracket, which made the image plane approximately orthogonal to the N-wires. Afterward, the bracket was mounted on the square grooves on the top of the phantom to allow its steady movement from the front to the back with the position sensor tracking in real time. Ultrasound images with the probe position were acquired by two distinct machines when the probe paused in arbitrary desired position and maintained the same pose.

2.4 Automatic Image Segmentation and Spot Detection

A set of clear ultrasound images was obtained after optimizing the phantom and the described acquisition method. A fast and completely automatic segmentation algorithm was performed to extract the N-fiducials. The proposed algorithm presented the following main steps:

Step 1. Gaussian Blur

Given the few bubbles present in the water bath, the speckles formed in the ultrasound image (Fig.3a) were smaller but nearer in brightness than those of N-fiducials (Fig.3e). A Gaussian blur process was applied to reduce the speckles' brightness. The speckle brightness after Gaussian blur approximated and considerably reduced, and the brightness of the edges in the concerned N-fiducials decreased. Consequently, all N-fiducials were brighter than any other speckle in the ultrasound images (Fig.3f).

ISSN 2616-5775 Vol. 3, Issue 3: 117-128, DOI: 10.25236/AJCIS.2020.030313

Step 2. Automatic Binarization

All N-fiducials can be easily distinguished from the speckles in the images based on their brightness. The dots became bright when the N-fiducials became close to the center of the dots. An image binarization process was used to extract all the N-fiducial regions. Notably, the number of N-fiducials in each B-scan image was fixed at 35 because of the multilayer N-wire phantom. According to this feature, a loop was performed to determine a suitable threshold initialized at 0.3, with a step size of 0.003 during image binarization. The loop continued until the number of connected objects in the binary image was 35. With this step, all the concerned dots were identified, and the speckles caused by noise were eliminated. (Fig.3b)

Step 3. Center Calculation

The N-fiducial, a region that contained multiple pixels, was represented by single centroid pixel to facilitate the calculation of subsequent calibration. This pixel was determined using two steps. First, the pixels of all connected objects were clustered. Afterward, each centroid coordinate (u_0, v_0) of the connected objects, where the N-fiducial was located, was calculated on the basis of the centroid formula, with consideration of all the clustered pixels:

$u_0 = \sum_i g_i u_i / G$	(1)
$v_0 = \sum_i g_i v_i / G$	(2)

where g_i is the grayscale of the ith pixel in the connected object, u_i is the lateral coordinate, v_i is the axial coordinate of the ith pixel in the connected object, and G is the sum of the grayscale of the connected object (Fig.3c).

Step 4. N-fiducial Sorting and Marking

With the use of the distinctive geometry of the multilayer N-wire phantom, the N-fiducials identified by the calculation step were sorted from the first layer to the seventh layer of N-wire, with each layer increasing from left to right. The N-fiducials were also marked with a distinct number. Consequently, regardless of the position of the phantom where the image was captured, each N-fiducial marked with the same number in the image corresponded to a point on the same N-wire in Fig.3d.

ISSN 2616-5775 Vol. 3, Issue 3: 117-128, DOI: 10.25236/AJCIS.2020.030313

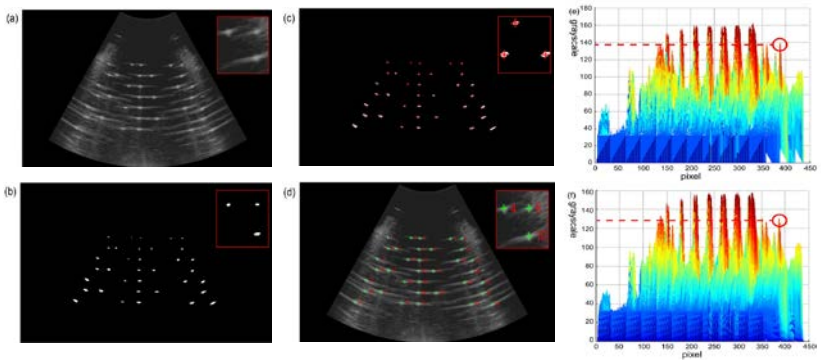

Fig. 3. Results from each step of the completely automatic segmentation algorithm. (a) Original ultrasound image with speckles. (b) Automatic binarization result. (c) Center calculation result (marked by a cross) . (d) Result after the final segmentation step during sorting and marking of N-fiducials. (e) Wireframe mesh of the original image. The speckle grayscale is relatively high (in red circles). (f) Wireframe mesh of the image after Gaussian blur. The speckle grayscale is remarkably reduced (in red circles).

2.5 Practical Freehand Ultrasound Geometric Calibration Method

1) Solution for R_{is} and T_{is} using singular value decomposition (SVD)

According to literature [9], The relationship between the coordinates of point P in sensor frame and image frame is as follows:

$F_i \rightarrow F_s : P_s = R_{is} \bullet P_i + T_{is}$	(3)

where R_{is} is a 3×3 rotation matrix, and T_{is} is a 3×1 translation vector from the image frame to the sensor frame. Here, P_i and P_s are both 3×14 coordinate matrices, and their covariance matrix H is expressed as follows:

$H = (P_s - m_s) \cdot (P_i - m_i)^T$	(4)

where m_i and m_s are the means of P_i and P_s, respectively. The covariance matrix H can be expressed as $U \cdot \sum \cdot V = SVD(H)$; this matrix is decomposed into three 3×3 matrices, namely, a normalized matrix U, a diagonal matrix $\sum$, and a matrix V, after SVD. Subsequently, a rotation matrix R_{is} and a translation matrix T_{is} can be calculated as follows:

$R_{is} = V \cdot U^T$,	(5)
$T_{is} = P_s - R_{is} \cdot P_i$,	(6)

where R_{is} and T_{is} are obtained by using (3)-(6).

ISSN 2616-5775 Vol. 3, Issue 3: 117-128, DOI: 10.25236/AJCIS.2020.030313

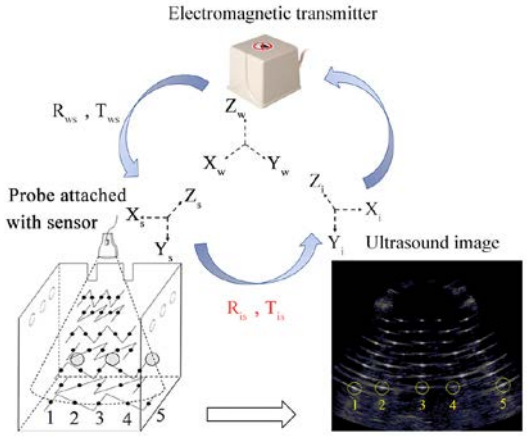

Fig.4 Relationship between the Ultrasound Image and the System Frames.

2)Determining R_{ws} and T_{ws} using distinct N-wire geometry

As shown in Fig.4, the coordinates of the makers in the image and electromagnetic frames in the N line can be obtained by using SVD with the N-wire model. The translation from the world frame to the sensor frame can be calculated with the parameter $[x, y, z, \alpha, \beta, \gamma]$ obtained from the electromagnetic tracking system, and the process can be shown as follows:

$F_w \rightarrow F_s : P_s = R_{ws} \bullet P_w + T_{ws}$	(7)

In detail, the rotation matrix R_{ws} can be computed through the Rodrigues formula as follows:

$R_{ws\_z} = \begin{pmatrix} \cos(\gamma) & -\sin(\gamma) & 0 \\ \sin(\gamma) & \cos(\gamma) & 0 \\ 0 & 0 & 1 \end{pmatrix}$	(8)
$R_{ws\_y} = \begin{pmatrix} \cos(\beta) & 0 & \sin(\beta) \\ 0 & 1 & 0 \\ -\sin(\beta) & 0 & \cos(\beta) \end{pmatrix}$	(9)
$R_{ws\_x} = \begin{pmatrix} 1 & 0 & 0 \\ 0 & \cos(\alpha) & -\sin(\alpha) \\ 0 & \sin(\alpha) & \cos(\alpha) \end{pmatrix}$	(10)
$R_{ws}=R_{ws\_x} \bullet R_{ws\_y} \bullet R_{ws\_z}$	(11)

The translation matrix is as follows:

ISSN 2616-5775 Vol. 3, Issue 3: 117-128, DOI: 10.25236/AJCIS.2020.030313

$T_{ws}=[x,y,z]$	(12)

After the automatic image segmentation, the coordinates of the three markers in each ultrasound image were obtained, and these three points were set as N_i, P_i, and Q_i, as shown in Fig.5. The endpoint of each N-wire was recorded as A_w, B_w, C_w, and D_w with the aid of an electromagnetic tracking system. Two similar triangles can be formed in the N-wire, and the similarity ratio is $\alpha=\|A_w-P_w\|/\|A_w-C_w\|=\|N_i-P_i\|/\|N_i-Q_i\|$, where $\|X-Y\|$ represents the absolute distance between points X and Y. Thus, the P_w coordinate in the world frame can be calculated as follows:

$P_w=A_w+\alpha\cdot(C_w-A_w)=A_w+(\|N_i-P_i\|/\|N_i-Q_i\|)\cdot(C_w-A_w)$	(13)

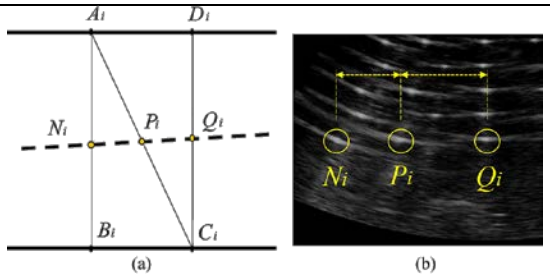

Fig. 5. N-wire model and marker points in the ultrasound image. (a) Top view of the N-wire model; the dashed line is the ultrasound plane, which intersects the N-wire at three marker points. (b) Three marker points.

3)Result forms

After automatic image segmentation, the coordinates of P_i and P_w in the image frame and the world frame can be computed as follows:

$P_i=\begin{pmatrix} x_{i1} & x_{i2} & \dots x_{in} & \dots & x_{i14} \\ y_{i1} & y_{i2} & \dots y_{in} & \dots & y_{i14} \\ 0 & 0 & \dots 0 & \dots & 0 \end{pmatrix}$	(14)
$P_w=\begin{pmatrix} x_{w1} & x_{w2} & \dots x_{wn} & \dots & x_{w14} \\ y_{w1} & y_{w2} & \dots y_{wn} & \dots & y_{w14} \\ z_{w1} & z_{w2} & \dots z_{wn} & \dots & z_{w14} \end{pmatrix}$	(15)

The points in the image frame presented no z coordinate. Hence, we used zero for the entire third row. A total of 14 sets of images indicated different sensor positions and P_w values, which resulted in different R_{ws} and T_{ws} values and ratios. With the use of (5), we acquired different values of P_s. Finally, the same R_{is} and T_{is} can be calculated by using SVD; these values corresponded to the

ISSN 2616-5775 Vol. 3, Issue 3: 117-128, DOI: 10.25236/AJCIS.2020.030313

relationship between the image frame of the ultrasound probe and the sensor fixed to the ultrasound probe.

2.6 Calibration Quality Assessment

(1) Evaluation of the calibration accuracy

Accuracy presents the deviation between the true value and the measurement, and it can be expressed by the fiducial reconstruction error (FRE): $FRE = \| \bar{x} - \tilde{x} \|$, where $\bar{\bullet}$ and $\tilde{\bullet}$ represent the true and the target values, respectively, in three different axes. Symbol $\| g \|$ denotes the norm value of g. We conducted N independent experiments. First, the same N-wire was scanned, and the image coordinate P_i of the markers was obtained. With the use of the same calibration result, the 3D coordinate P_w of the markers in the world frame was calculated. The real P_{wa} position can be computed by using (8). Therefore, the calibration accuracy value can be acquired as follows: $FRE = \| P_w - P_{wa} \|$.

(2)Evaluation of calibration precision

Precision refers to the consistency of the results obtained in a number of experiments and indicates the repeatability and robustness of the algorithm. After collecting 14 sets of data, we repeated the calculation of calibration for N times and recorded each calibration outcome as T_i. In the precision experiment, we selected the center and corners points on the ultrasound image as the recorded data. The precision was evaluated by the following calibration reproducibility (CR): $CR = \frac{1}{N} \sum_{i=1}^{N} \left\| \bar{\mathrm{X}}_i - T_i \bullet \mathrm{X}_i \right\|$, where $\bar{\mathrm{X}}_i = \frac{1}{N} \sum_{i=1}^{N} T_i \bullet \mathrm{X}$.

3. Results

3.1 Segmentation Performance

We collected 40 images at random locations on the multilayer N-wire phantom for a total of 560 N-fiducials. These images served as input, and they were segmented by the automatic segmentation algorithm. All N-fiducials were accurately identified. No dot caused by noise was misidentified as N-fiducial. This result indicated that the algorithm was relatively robust.

3.2 Evaluation of Calibration Precision

We randomly divided 40 images into five groups with eight images; each set was an independent experiment. First, we calculated the calibration parameters for each

ISSN 2616-5775 Vol. 3, Issue 3: 117-128, DOI: 10.25236/AJCIS.2020.030313

group separately, as well as the precision and accuracy. The point reconstruction of five selected points (one center and four corners) in the same ultrasound image (720×440 pixels) by five calibrations and CR of five selected points is shown in Table I and Fig.7. The accuracy (evaluated by FRE) of the calibration is presented in Table II.

The CR and FRE are approximately similar in all trials, and the average CR and FRE are 1.29 and 1.42 mm, respectively. As shown in Table III, our precision is significantly better than those of related works, and the accuracy is consistent with that of N-wire phantom used in the literature [10]. The use of phantomless method [11] achieves slightly improved accuracy. Notably, the phantomless method presents a restriction on data acquisition protocol and the cost of complexity during feature extraction. A significant advantage of our phantom is that the FRE converges to a small value with a few images. We found that only eight images with a total of 112 N-fiducials can be used to converge the FRE to a stable value.

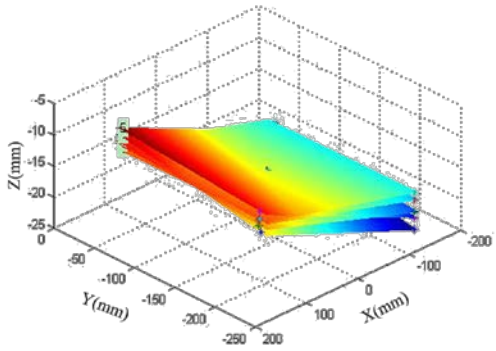

Fig.7 The Point Reconstruction of Five Selected Points (One Center and Four Corners) in the Same Ultrasound Image (720×440 Pixels) by Five Calibrations.

Table 1 Calibration Reproducibility (Cr) of Five Selected Points

Point	Left (top)	Right (top)	Left (down)	Right (down)	Center	Average
CR (mm)	1.17	1.04	1.32	2.20	0.73	1.29

Table 2 Fiducial Reconstruction Error (Fre) of Five Trials

Trial number	1	2	3	4	5	Average
FRE (mm)	1.02	1.87	1.59	1.73	0.91	1.42

Table 3 Comparison of Precision and Accuracy with Those of Related Works

ISSN 2616-5775 Vol. 3, Issue 3: 117-128, DOI: 10.25236/AJCIS.2020.030313

Phantom	Precision (CR) (mm)	Accuracy (FRE) (mm)
Multilayer N-wire phantom (our work)	1.29	1.42
N-wire phantom [10]	2	1.40
Phantomless [11]	-	1.20

4. Conclusion

Ultrasound geometric calibration is the fundamental issue in freehand ultrasound system. The calibration quality exerts considerable influence on the function of the whole system. In our research, we propose an improved automatic calibration method that combines electromagnetic tracking and ultrasound. We systematically describe the geometry of the phantom and the auxiliary bracket used to hold the probe during data acquisition. We also propose a completely automatic image segmentation algorithm that requires no human intervention in extracting N-fiducials. Results of extensive experiments showed that only eight images from each experiment are needed to obtain highly precise and accurate calibration result with minimal human interaction and without the need for temporal calibration. The accuracy is also acceptable in labor guidance and other applications.

Acknowledgement

This work was funded and supported by the National Key Research and Development Project (2019YFC0120100 and 2019YFC0121907).

References

[1] O. Dupuis, S. Ruimark, D. Corinne, et al (2005). Fetal head position during the second stage of labor: Comparison of digital vaginal examination and transabdominal ultrasonographic examination. Eur J Obstet Gynecol Reprod Biol, vol.123, no.2, p. 193-197.

[2] E. L. Melvaer, K. Morken and E. Samset (2012). A motion constrained cross-wire phantom for tracked 2D ultrasound calibration. Int J Comput Assist Radiol Surg, vol.7, no.4, p. 611-620.

[3] J. Kowal, C. A. Amstutz, Caversaccio M, et al. (2003). On the development and comparative evaluation of an ultrasound B-mode probe calibration method. Comput Aided Surg, vol.8, no.3, p. 107-119.

[4] D. F. Leotta (2004). An efficient calibration method for freehand 3-D ultrasound imaging systems. Ultrasound Med Biol, vol.30, no.7, p. 999-1008.

[5] R. W. Prager, R. N. Rohling, A. H. Gee and L. Berman (1998). Rapid calibration for 3-D freehand ultrasoun. Ultrasound Med Biol, vol. 24, no.6, p. 855-869.

ISSN 2616-5775 Vol. 3, Issue 3: 117-128, DOI: 10.25236/AJCIS.2020.030313

[6] R. M. Comeau, A. F. Sadikot, A. Fenster and T. M. Peters (2000). Intraoperative ultrasound for guidance and tissue shift correction in image-guided neurosurgery. Med Phys, vol. 27, no.4, p. 787-800.
[7] T. K. Chen, A. D. Thurston, R. E. Ellis and P. Abolmaesumi (2009). A real-time freehand ultrasound calibration system with automatic accuracy feedback and control. Ultrasound Med Biol, vol.35, no.1, p. 79-93.
[8] P. W. Hsu, R. W. Prager, A. H. Gee, G. M. Treece, et al. (2008). Real-time freehand 3D ultrasound calibration. Ultrasound Med Biol, vol. 34, no.2, p. 239-251.
[9] RQ Yang, ZG Wang, SJ Liu and XM Wu (2013). Design of an Accurate Near Infrared Optical Tracking System in Surgical Navigation. J Lightwave Technol, vol.31, no.2, p. 223-231.
[10] G. Carbajal, A. Lasso, Á. Gómez and G. Fichtinger (2013). Improving N-wire phantom-based freehand ultrasound calibration. Int J Comput Assist Radiol Surg, vol.8, no.6, p. 1063-1072.
[11] M. Toews and W. M. Wells (2018). Phantomless Auto-Calibration and Online Calibration Assessment for a Tracked Freehand 2-D Ultrasound Probe. IEEE Trans Med Imaging, vol.37, no.1, p. 262-272.